

## Article

# Hydrodynamics of an Elliptical Squirmer

Chen Liu <sup>1</sup>, Peijie Zhang <sup>1</sup>, Jianzhong Lin <sup>1,2,\*</sup>  and Zhenyu Ouyang <sup>1</sup>

<sup>1</sup> State Key Laboratory of Fluid Power Transmission and Control, Zhejiang University, Hangzhou 310027, China; 12024039@public.zju.edu.cn (C.L.); pjzhang@zju.edu.cn (P.Z.); ouyangzhenyu@zju.edu.cn (Z.O.)

<sup>2</sup> Laboratory of Impact and Safety Engineering, Ningbo University, Ministry of Education, Ningbo 315201, China

\* Correspondence: mecjzlin@public.zju.edu.cn

**Abstract:** In this paper the propulsion of elliptical objects (called squirmers) by imposed tangential velocity along the surface is studied. For a symmetric velocity distribution (a neutral squirmer), pushers (increased tangential velocity on the downstream side of the ellipse) and pullers (increased tangential velocity on the upstream side of the ellipse), the hydrodynamic characteristics, are simulated numerically using the immersed boundary-lattice Boltzmann method. The accuracy of the numerical scheme and code are validated. The effects of Reynolds number (Re) and squirmer aspect ratio (AR) on the velocity  $u^*$ , power expenditure  $P^*$  and hydrodynamic efficiency  $\eta$  of the squirmer are explored. The results show that the change of  $u^*$  along radial direction  $r^*$  shows the relation of  $u^* \sim r^{*-2}$  for the neutral squirmer, and  $u^* \sim r^{*-1}$  for the pusher and puller. With the increase of Re,  $u^*$  of the pusher increases monotonically, but  $u^*$  of the puller decreases from Re = 0.01 to 0.3, and then increases from Re = 0.3 to 3. The values of  $P^*$  of the pusher and puller are the same for  $0.01 \leq \text{Re} \leq 0.3$ ;  $P^*$  of the pusher is larger than that of the puller when  $\text{Re} > 0.3$ .  $\eta$  of the pusher and puller increases with increasing Re, but the pusher has a larger  $\eta$  than the puller at the same Re.  $u^*$  and  $P^*$  decrease with increasing AR, and the pusher and puller have the largest and least  $u^*$ , respectively. The values of  $P^*$  of the pusher and puller are almost the same and are much larger than those of the neutral squirmer. With the increase of AR,  $\eta$  increases for the neutral squirmer, but changes non-monotonically for the pusher and puller.

**Keywords:** elliptical squirmer; velocity; power expenditure; hydrodynamic efficiency; IB-LBM



**Citation:** Liu, C.; Zhang, P.; Lin, J.; Ouyang, Z. Hydrodynamics of an Elliptical Squirmer. *Processes* **2022**, *10*, 805. <https://doi.org/10.3390/pr10050805>

Academic Editor: Leila Pakzad

Received: 15 March 2022

Accepted: 15 April 2022

Published: 19 April 2022

**Publisher's Note:** MDPI stays neutral with regard to jurisdictional claims in published maps and institutional affiliations.



**Copyright:** © 2022 by the authors. Licensee MDPI, Basel, Switzerland. This article is an open access article distributed under the terms and conditions of the Creative Commons Attribution (CC BY) license (<https://creativecommons.org/licenses/by/4.0/>).

## 1. Introduction

Self-driven particles such as microorganisms and synthesized particles widely exist in nature and actual applications. Swimming and transporting nutrition in the biofluids are basic survival needs of microorganisms (e.g., spermatozoa, bacillus). They gather in a place full of nutrients, breed and build territory. On the other hand, synthesized self-driven particles (e.g., artificial cell, Janus, biomarkers, miniature swimming devices) are designed for targeted drug delivery, precise surgery and so on [1]. The swimming mode of the self-driven particles can mostly be described by the squirmer model which was initially proposed by Lighthill [2] based on the Opalina propulsion mode in the three-dimensional (3D) status. Moreover, Blake has modified the 3D model [3] and built the 2D circular squirmer model [4].

The spherical squirmer model has been adopted in many research studies and its feasibility has been confirmed as well. Ishikawa and Pedley used the 3D squirmer model to study the coherent structure of a single-layer spherical particle suspension and found it was induced by hydrodynamic interactions [5]. For the mass transportation of the squirmer, the hovering and migrating could be attributed to the mass transfer [6]. For the interaction between two squirmers, the squirmers would make contact with each other at the beginning, and then change their swimming directions, and finally draw apart [7]. For the rheological

properties of semi-dilute squirmer suspension, it was discovered that the deviation of the mass center of the squirmers contributed to the change of the apparent viscosity of the suspension [8]. Ouyang et al. found that the existence of shear-thinning effect reduced the squirmer speed and decreased its power expenditure [9]. They also investigated the interaction between a squirmer and the wall, and the interaction of two squirmers [10,11]. The former focused on the effect of the power-law index,  $Re$ , and position of the squirmer with respect to the wall on the squirmer motion; the latter focused on the relative motion state of two squirmers. Moreover, it was presented that a rod squirmer in a channel flow appeared with four different swimming modes at different  $Re$ , blockage ratio and self-driven mode of the squirmer [12].

Besides spherical self-driven particles, many researchers also paid attention to the axisymmetric self-driven particles. Zantop and Stark [13] constructed a claviform squirmer by linearly arranging several spherical squirmers and introducing a new velocity model for it. Ouyang et al. [14,15] studied the hydrodynamic behaviors of a rod squirmer assembled by several circular squirmers in the flows with different rheological property, and a more complex method was used to derive the velocity of the squirmer with a different shape. Inspired by Blake's effort in modeling the mode of spherical ciliated microorganisms [3,16,17], Keller and Wu [18] proposed a model for prolate-spheroidal ciliated squirmers, and the numerical result of the streamline matched qualitatively with the experimental one. However, Theers et al. [19] pointed out that Keller and Wu's model just considered the swimming mode but ignored the force-dipole mode which decided the interaction between squirmers, or between the squirmer and the wall. Thus, they took force-dipole into account and offered another mode which was also suitable in the variable temperature flow. In subsequent work, the model was expanded to the situation of clustering of spheroidal squirmers [20] and was widely used to explore the collective motion. Shapere and Wilczek [21] made an effort to search for the most efficient Stokes for deformable squirmers. They used a conformal-mapping technique to deal with the unknown swimming velocity for squirmers with different shapes. Leshansky et al. [22] used the conformal-mapping technique to map the shapes of ellipsoid and ellipse squirmers onto sphere and circle, and they obtained an optimal swimming mode. In their study, they obtained the relevant tangential velocity based on the assumption of the lowest dissipation rate, and the direction of the squirmer's velocity needed an additional solution in numerical calculation. It is necessary to obtain the tangential velocity without such an assumption, and one must directly assign velocity to the particle boundary without looking for the corresponding tangential direction. This is one of the motives of this paper.

Inspired by the previous works mentioned above, this work aims at proposing a tangential velocity model for the elliptical squirmer based on the circular squirmer model and the conformal-mapping technique. With a second-order immersed boundary-lattice Boltzmann method (IB-LBM), the hydrodynamic characteristics of the elliptical squirmer are simulated numerically. The present study has two goals: one is to build a new velocity model which is applicable for simulating the movement of the elliptical squirmer; the other is to clarify the ways in which the  $Re$  and aspect ratio (AR) of the squirmer affect the movement of the elliptical squirmer, and reveal the corresponding hydrodynamic mechanism.

## 2. Numerical Method and Swimming Model of Squirmer

The IB-LBM is used in the simulation. The LBM and IB are applied to solve the flow motion and deal with the boundary condition, respectively.

### 2.1. Lattice Boltzmann Method

A squirmer swimming in a viscous and incompressible flow can be described by the lattice Boltzmann equation with an external forcing term:

$$f_{\alpha}(\mathbf{x} + \mathbf{e}_{\alpha}\Delta t, t + \Delta t) = f_{\alpha}(\mathbf{x}, t) - \frac{1}{\tau} \left[ f_{\alpha}(\mathbf{x}, t) - f_{\alpha}^{eq}(\mathbf{x}, t) \right] + F_{\alpha}(\mathbf{x}, t)\Delta t, \quad (1)$$

where  $f_\alpha(x, t)$  is the distribution function of particle in the  $\mathbf{x}$  position and  $\mathbf{e}_\alpha$  direction at time  $t$ ;  $\tau$  is the dimensionless relaxation time;  $\Delta t$  is the unit lattice time;  $F_\alpha(\mathbf{x}, t)$  is the discrete force distribution function;  $f_\alpha^{eq}(\mathbf{x}, t)$  is the equilibrium distribution function and can be expressed as:

$$f_\alpha^{eq}(\mathbf{x}, t) = w_\alpha \rho \left[ 1 + \frac{(\mathbf{e}_\alpha \cdot \mathbf{u})}{c_s^2} + \frac{(\mathbf{e}_\alpha \cdot \mathbf{u})^2}{2c_s^4} - \frac{\mathbf{u}^2}{2c_s^2} \right], \quad (2)$$

where  $\rho$  is the fluid density;  $\mathbf{u}$  is the fluid velocity;  $w_\alpha$  is the weight associated with the  $\mathbf{e}_\alpha$ ;  $c_s$  is the sound speed and can be calculated by the lattice speed  $c$  as  $c_s = c/\sqrt{3}$ .

The nine-velocity (D2Q9) model is used to discretize velocity space, and the particle velocities  $\mathbf{e}_\alpha$  and  $w_\alpha$  are defined as:

$$\mathbf{e}_\alpha = \begin{cases} (0, 0) & \alpha = 0 \\ (\pm 1, 0), (0, \pm 1) & \alpha = 1, 2, 3, 4 \\ (\pm 1, \pm 1) & \alpha = 5, 6, 7, 8 \end{cases}, \quad w_\alpha = \begin{cases} 4/9 & \alpha = 0 \\ 1/9 & \alpha = 1, 2, 3, 4 \\ 1/36 & \alpha = 5, 6, 7, 8 \end{cases} \quad (3)$$

The discrete force distribution function  $F_\alpha(\mathbf{x}, t)$  is expressed as [23]:

$$F_\alpha(\mathbf{x}, t) = \left( 1 - \frac{1}{2\tau} \right) w_\alpha \left[ \frac{\mathbf{e}_\alpha - \mathbf{u}(\mathbf{x}, t)}{c_s^2} + \frac{\mathbf{e}_\alpha \cdot \mathbf{u}(\mathbf{x}, t)}{c_s^4} \mathbf{e}_\alpha \right] \cdot \mathbf{f}(\mathbf{x}, t), \quad (4)$$

where  $\mathbf{f}(\mathbf{x}, t)$  is the external force density and needs to be computed in advance; thus, fluid density and velocity can be calculated as:

$$\rho = \sum_\alpha f_\alpha, \quad \rho \mathbf{u} = \sum_\alpha \mathbf{e}_\alpha f_\alpha + \frac{\Delta t}{2} \mathbf{f}. \quad (5)$$

## 2.2. Direct-Forcing Immersed Boundary Method

Two grids were chosen to obtain the solution of  $\mathbf{f}(\mathbf{x}, t)$  as shown in Figure 1; one is the Lagrangian grid, where the boundary of the squirmer is represented by Lagrangian points (subscript  $b$ ); the other is a Eulerian grid, and Eulerian points correspond to the fluid points (subscript  $f$ ). Then,  $\mathbf{f}(\mathbf{x}, t)$  can be obtained by:

$$\mathbf{f}_f(\mathbf{x}_f, t) = \sum_b \mathbf{F}_b(\mathbf{x}_b, t) D(\mathbf{x}_f - \mathbf{x}_b) \Delta s_b, \quad (6)$$

where  $D$  is the discrete delta function;  $\Delta s_b$  is the arc length of the boundary segment;  $\mathbf{F}_b(\mathbf{x}_b, t)$  is the force density exerted on the boundary of the squirmer at point  $\mathbf{x}_b$  and time  $t$ , which can be expressed as:

$$\mathbf{F}_b(\mathbf{x}_b, t + \Delta t) = 2\rho_b^{noF}(\mathbf{x}_b, t + \Delta t) \frac{\mathbf{U}_b^d - \mathbf{u}_b^{noF}(\mathbf{x}_b, t + \Delta t)}{\Delta t}, \quad (7)$$

where  $\mathbf{u}_b^{noF}$  and  $\rho_b^{noF}$  are the unforced velocity and density at Eulerian point  $\mathbf{x}_b$ , and can be calculated by:

$$\mathbf{u}_b^{noF}(\mathbf{x}_b, t) = \sum_f \mathbf{u}_f^{noF}(\mathbf{x}_f, t) D(\mathbf{x}_f - \mathbf{x}_b) h^2, \quad \rho_b^{noF}(\mathbf{x}_b, t) = \sum_f \rho_f^{noF}(\mathbf{x}_f, t) D(\mathbf{x}_f - \mathbf{x}_b) h^2 \quad (8)$$

where  $h$  is the mesh spacing  $h = \Delta x$ .

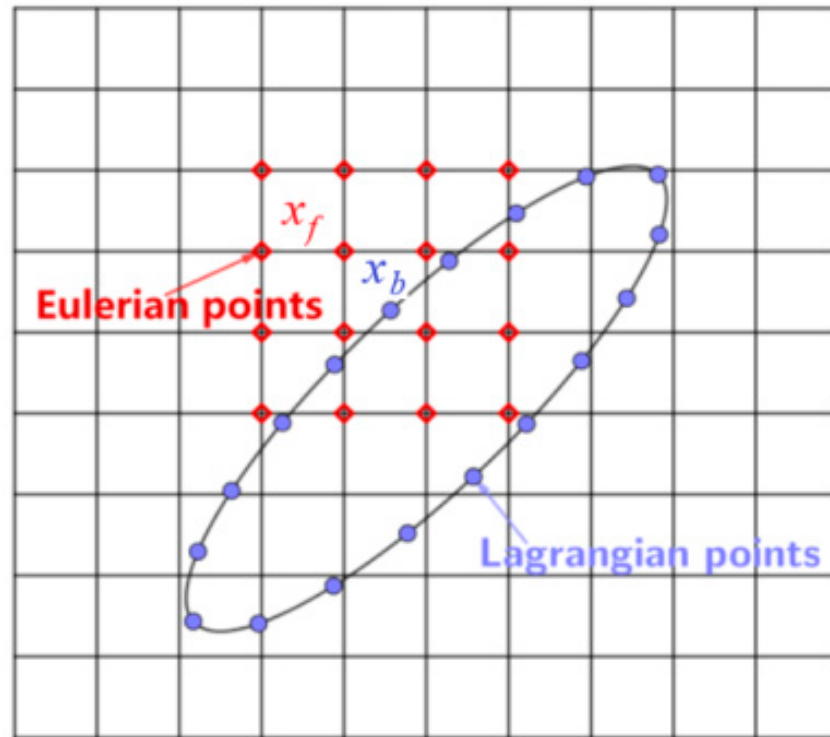


**Figure 1.** Schematic of the Eulerian and Lagrangian grids.

$D$  is used to establish the connection between the fluid and the immersed boundary. Here, a smoothed four-point piecewise function proposed by Yang et al. [24] is adopted for its second-order accuracy:

$$D(\mathbf{x}_f - \mathbf{x}_b) = \frac{1}{h^2} \delta\left(\frac{x_f - x_b}{h}\right) \delta\left(\frac{y_f - y_b}{h}\right), \quad (9)$$

$$\delta(r) = \begin{cases} \frac{3}{8} + \frac{\pi}{32} - \frac{r^2}{4}, & |r| \leq 0.5 \\ \frac{1}{4} + \frac{1-|r|}{8} \sqrt{-2 + 8|r| - 4r^2} - \frac{1}{8} \arcsin(\sqrt{2}(|r| - 1)), & 0.5 < |r| \leq 1.5 \\ \frac{17}{16} - \frac{\pi}{64} + \frac{|r|-2}{16} \sqrt{-14 + 16|r| - 4r^2} + \frac{1}{16} \arcsin(\sqrt{2}(|r| - 2)) + \frac{r^2}{8} - \frac{3|r|}{4}, & 1.5 < |r| \leq 2.5 \\ 0, & |r| \geq 2.5 \end{cases} \quad (10)$$

### 2.3. The Velocity Model of the Elliptical Squirmer

Based on the circular squirmer model [4,25], a tangent velocity model of the elliptical squirmer is built. This model is suitable for a rigid, elliptical squirmer swimming slowly in an incompressible, infinite flow by its surface pedal motion.

The movement of an elliptical squirmer in the complex plane  $z = x + iy$  is considered. For convenience, the mass center, semi-major axis  $a$  and semi-minor axis  $b$  of the squirmer are used to establish the center-of-mass frame, corresponding to the center,  $x$ - and  $y$ -axis, respectively. Using  $z = \zeta + \alpha/\zeta$  ( $a = 1 + \alpha$ ,  $b = 1 - \alpha$  ( $0 \leq \alpha < 1$ )) for conformal mapping as shown in Figure 2, the ellipse in  $z$ -plane can be transformed into a unit circle (the surface of  $\zeta = e^{i\theta}$ ,  $\theta$  is the argument of any point on the surface) in  $\zeta$ -plane.  $\zeta$  is further defined as  $\zeta = m + in$  for simplifying. This mapping keeps the tangent relationship of any point on the squirmer's surface and its surface velocity in two different planes.

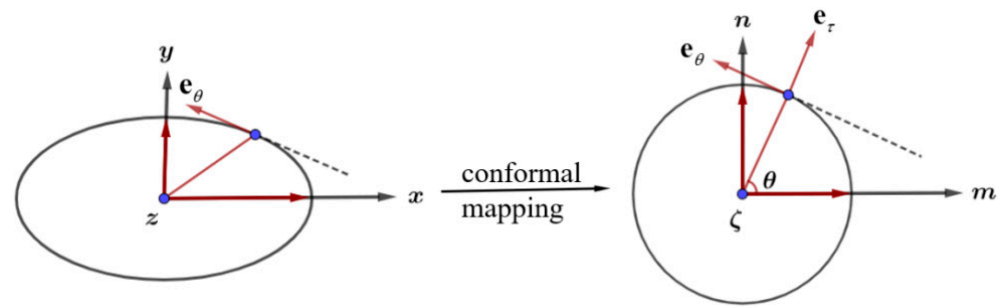


Figure 2. Schematic of the process of the conformal mapping from  $z$ -plane to  $\zeta$ -plane.

According to the conformal mapping, we have:

$$x + iy = m + in + \frac{\alpha}{m + in}, \quad (11)$$

and the transformation relation between coordinates can be obtained:

$$\begin{cases} x = m(1 + \alpha) \\ y = n(1 - \alpha) \end{cases}, \quad (12)$$

according to the definition of velocity magnitude, i.e.,  $v = ds/dt$ , the relationship between velocity component values in two planes is:

$$\begin{cases} v_x = v_m(1 + \alpha) \\ v_y = v_n(1 - \alpha) \end{cases}, \quad (13)$$

where subscript  $x$  and  $y$  mean the parameters along  $x$  and  $y$  direction in  $z$ -plane;  $m$  and  $n$  mean the parameters along  $m$  and  $n$  direction in  $\zeta$ -plane.

An elliptical squirmer swims freely in a static and finite flow under the induction of its surface velocity  $\mathbf{v}$ . After a period of initial motion, the squirmer will swim steadily with velocity  $\mathbf{U} = U\mathbf{e}_x$ . Meanwhile, the unit circular squirmer in  $\zeta$ -plane will correspondingly reach its final stable velocity  $U/(1 + \alpha)$ . The surface velocity can be simplified as  $\mathbf{v}_\theta = v_\theta\mathbf{e}_\theta$  ( $v_\theta = B_1\sin\theta + 2B_2\sin\theta\cos\theta$ ) [9], and  $B_1$  and  $B_2$  are specified constants. It is called a neutral swimmer if  $B_2 = 0$ , a pusher if  $B_2 < 0$  and a puller if  $B_2 > 0$ . When particle  $Re$  tends to 0, the velocity of the squirmer center mass would be closer to the constant  $B_1/2$  along the swimming direction of the squirmer, which is from the analytic result and has been explained in detail in [4,9].

#### 2.4. Swimming Power and Hydrodynamic Efficiency

The swimming power of a squirmer can be defined as [14]:

$$P = - \int_S \mathbf{n} \cdot \boldsymbol{\sigma} \cdot (\mathbf{u} + \mathbf{v}_\theta) dS, \quad (14)$$

where  $\mathbf{n}$  is the unit normal vector outward from the squirmer surface  $S$ ,  $\boldsymbol{\sigma}$  is the stress tensor,  $\mathbf{u}$  is the translational velocity of the elliptical squirmer in the laboratory frame and  $\mathbf{v}_\theta$  is the tangential velocity used at the boundary.

The expression of hydrodynamic efficiency of a squirmer swimming with stable velocity  $U$  is [26]:

$$\eta = \frac{4\pi\mu U^2}{P}. \quad (15)$$

### 3. Results and Discussion

#### 3.1. Validation of Numerical Scheme

The numerical case of catching the trajectory of a passive circular particle in a shear flow is presented to validate the accuracy of IB-LBM and the numerical scheme. As shown in Figure 3, a particle with radius of  $a$  is initially located at the flow; the variation of particle lateral position  $y$  with time  $t$  can be given when the particle moves. The computation domain is  $L = 200a$  and  $H = 8a$ . The flow and particle  $Re$  are  $Re_b = U_w H / \nu = 40$  and  $Re_p = U_w a^2 / (\nu H) = 0.625$ , respectively. The numerical result of the relationship between  $y/H$  and  $t^* = U_w t / L$  is shown in Figure 4 where other numerical results  $\blacktriangle$  [27],  $\blacktriangledown$  [28] and  $\bullet$  [29] are also given as comparison. It can be seen that the present numerical results are in good agreement with other results.

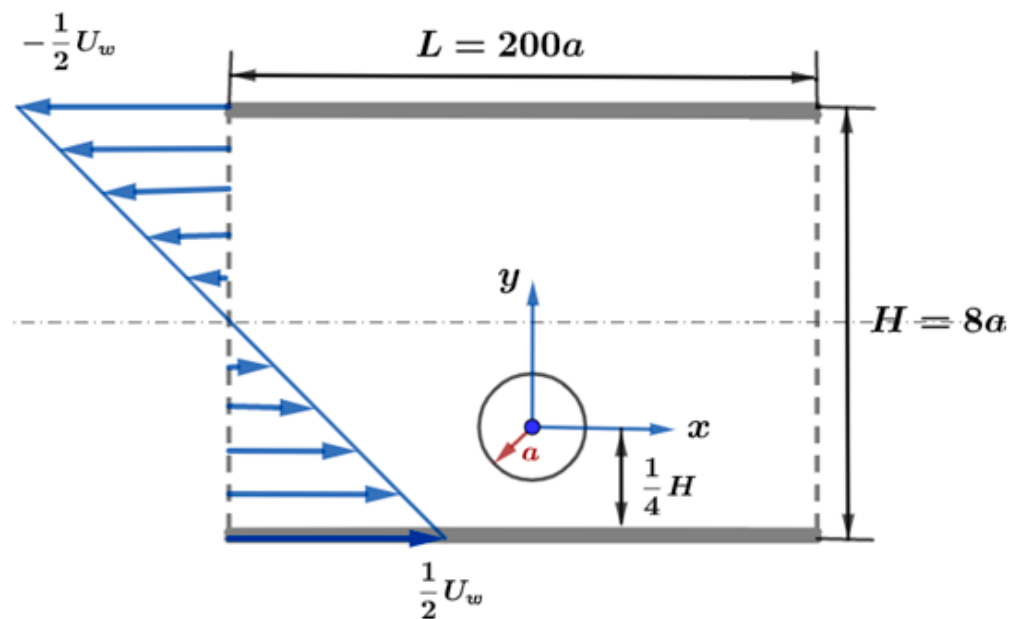


Figure 3. A particle in a shear flow.

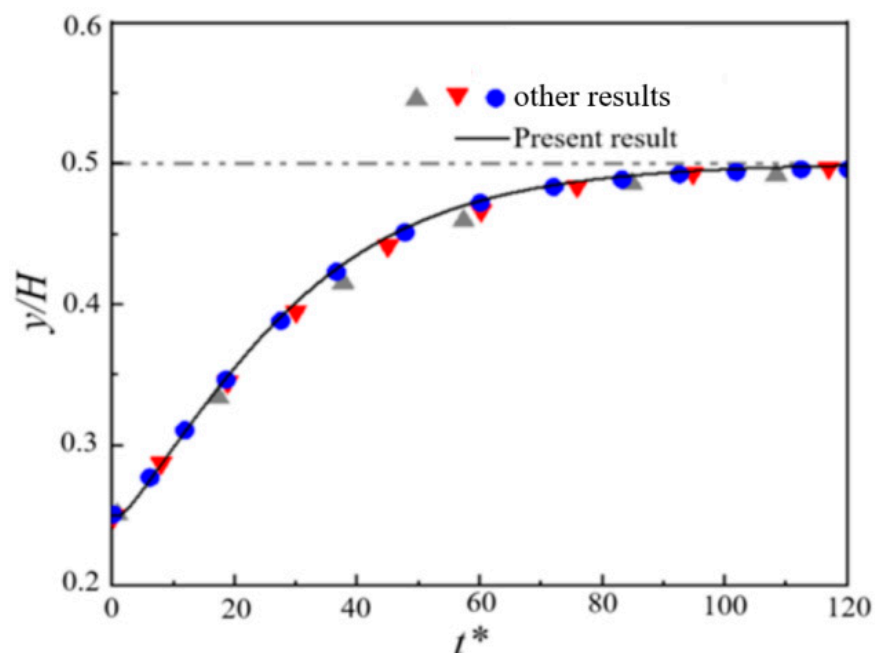


Figure 4. Comparison of trajectory in a shear flow.

### 3.2. Flow Induced by the Squirmer

The locomotion of an elliptical squirmer in an infinite flow is simulated numerically. The squirmer is initially placed at the center of the flow with its long axis parallel to the  $x$ -axis and moves along  $x$  positive direction by treadingmilling. The size of the computational domain is  $H \times L = 500\delta x \times 800\delta y$  ( $\delta x$  and  $\delta y$  are grid size), which is confirmed to be big enough to ignore the influence of boundaries. Moving mesh technology is applied, and the grid independence test has been performed. Re is defined as  $Re = 2\rho U_c r_c / \mu = \rho B_1 r_c / \mu$ , where  $U_c$  is swimming velocity of the squirmer,  $\rho$  is fluid density,  $\mu$  is fluid viscosity and  $r_c$  is equivalent radius of the squirmer ( $\pi r_c^2 = \text{area of the elliptical squirmer}$ ).  $AR = b/a = (1 - \alpha)/(1 + \alpha)$  ( $0 \leq \alpha < 1$ ).

Streamline and velocity induced by the elliptical squirmer with different AR at  $Re = 0.01$  are shown in Figure 5 where the black arrows indicate the direction of squirmer swimming, and dark black lines represent flagella on the head and tail of the squirmer. We can see that, for the neutral squirmer in (a), the streamline and velocity are fore-aft symmetric, and there are some differences in the shape of streamline distribution for the squirmer with different AR because the slip velocity component is related to  $\alpha$  ( $AR = (1 - \alpha)/(1 + \alpha)$ ), which is consistent with the conclusion in the rod squirmer [13]. The flows induced by a pusher or puller as shown in (b) and (c) agree with that for ellipsoid squirmers [19,30,31].

For a pusher as shown in (c), the fluid travels away from its two poles (where  $v_\theta$  changes sign [32]) and moves toward its two sides directly, like sperm cells spinning the flagella of the tail to push the body swimming ahead. As for a puller as shown in (b), the opposite is true; the puller moves like *Chlamydomonas* pushing away the fluid ahead of them and moving by the dragging of two flagella on the head. In fact, the velocity distribution in (b) and (c) should also be fore-aft symmetric like that in (a), but it was not because the inertia will destroy this symmetry. In addition, the velocity increases with increasing AR, which also needs to be clarified further.

Velocity decay of the squirmer along the radial direction with different AR is shown in Figure 6 where  $u^* = |u|/U$  and  $r^* = r/2a$  (here, radial direction is the swimming direction of the squirmer as shown with black arrows in Figure 5); symbols are the numerical results and the lines represent the exponential fitting of the numerical results. It can be seen that the results of velocity decay are close to the results for the rod squirmer given by Blake [4], i.e., the curves are  $u^* \sim r^{*-2}$  for the neutral squirmer, and  $u^* \sim r^{*-1}$  for the pusher and puller.

### 3.3. Effect of Reynolds Number

When the squirmer's motion reaches a steady state, the vortical contours induced by the squirmer with different Re are shown in Figure 7 where solid and dashed lines represent positive and negative vorticity, respectively, and contour range is  $-10^{-5} \sim 10^{-5}$  for  $Re = 0.01$  and  $-10^{-3} \sim 10^{-3}$  for other Re. The distribution of position, shape and density of vortical contours can reflect the change of flow caused by the squirmer when swimming. Through this change, we can also understand the swimming characteristics of the squirmer.

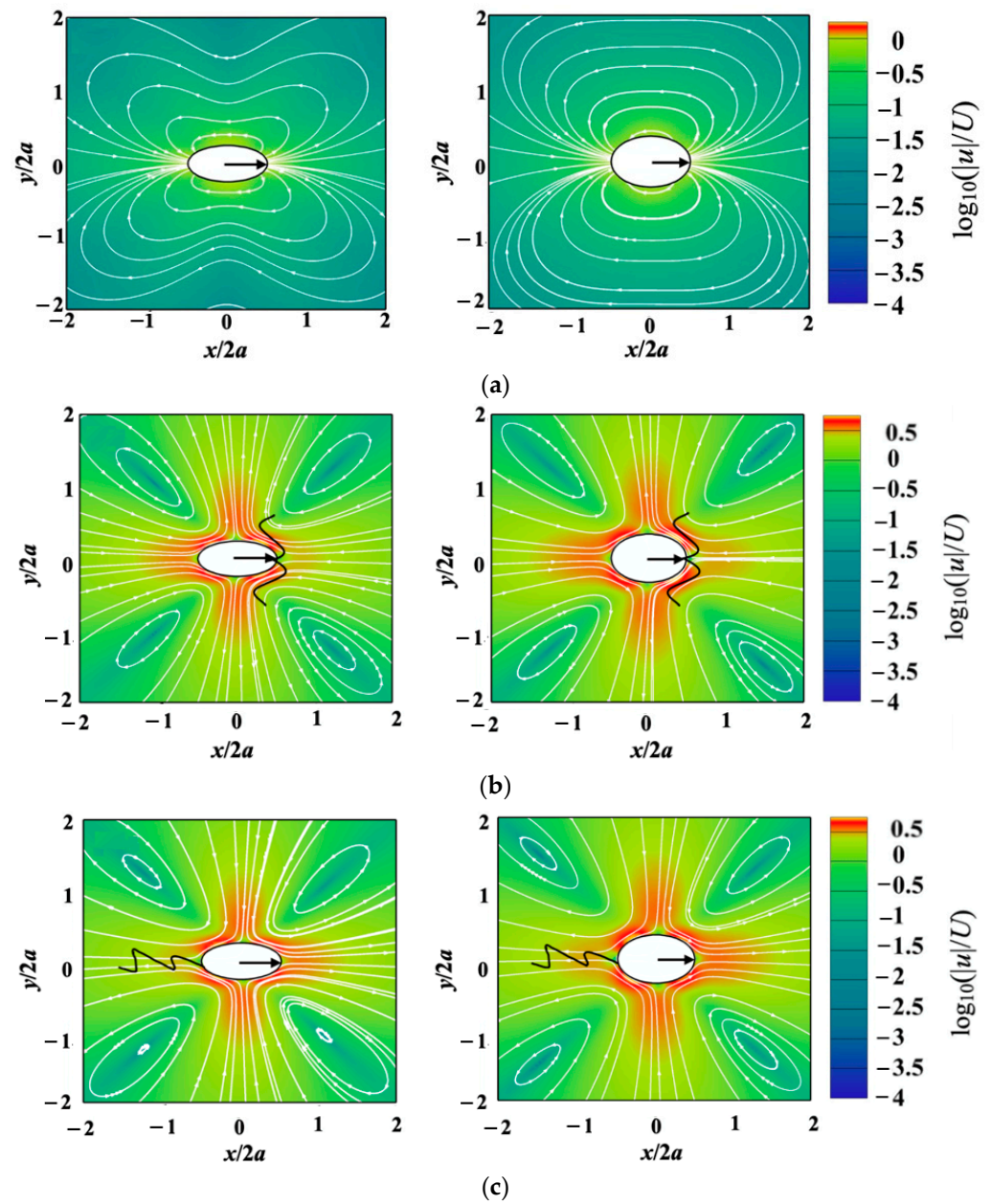


Figure 5. Streamline and velocity (color) induced by squirmer with AR = 0.5 (left) and 0.7(right). (a) neutral squirmer ( $\beta = 0$ ). (b) puller ( $\beta = 5$ ). (c) pusher ( $\beta = -5$ ).

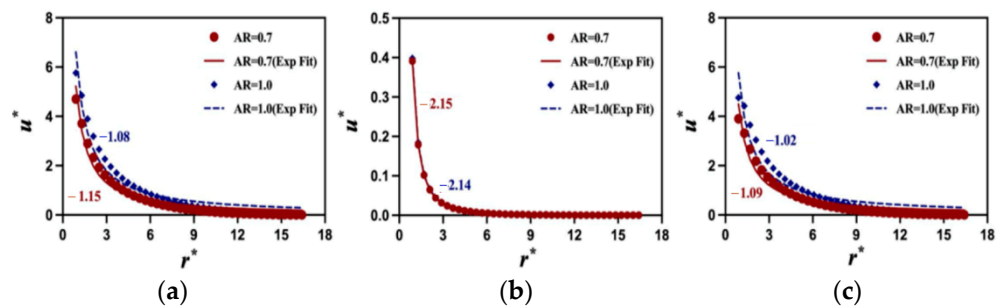
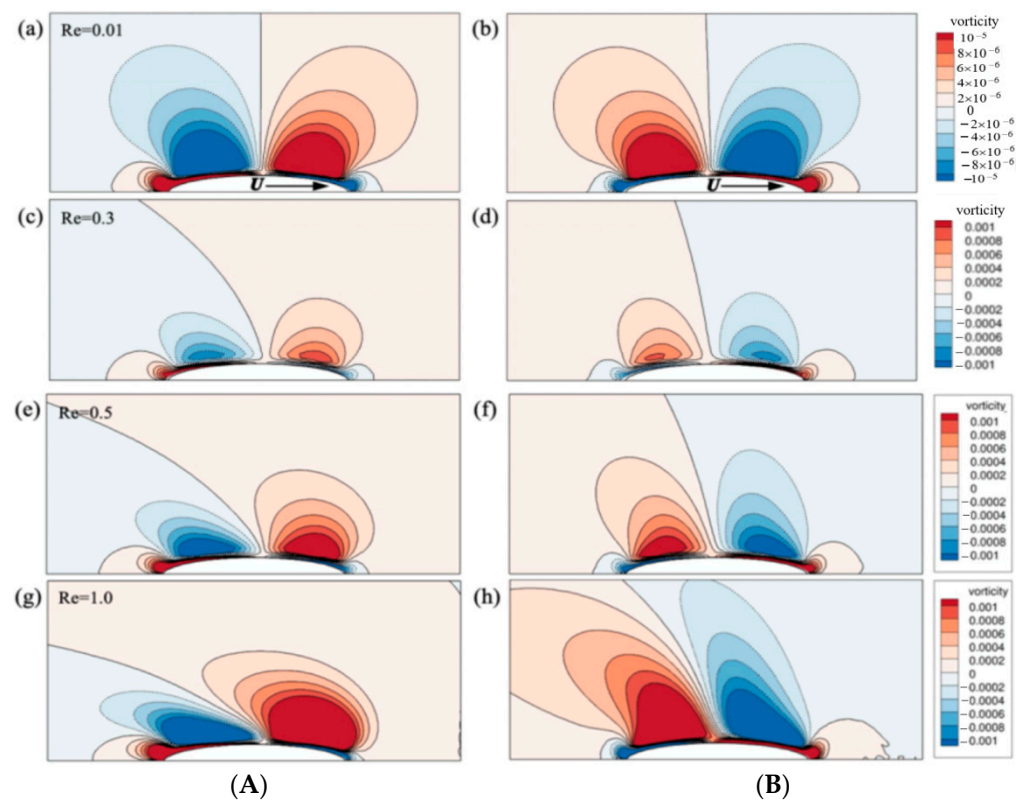


Figure 6. Velocity decay of elliptical squirmer along radial direction. (a) pusher ( $\beta = -5$ ). (b) neutral squirmer ( $\beta = 0$ ). (c) puller ( $\beta = 5$ ).



**Figure 7.** Vortical contours induced by elliptical squirmer with different  $Re$  for  $AR = 0.2$ . (a,b)  $Re = 0.01$ , (c,d)  $Re = 0.3$ , (e,f)  $Re = 0.5$ , (g,h)  $Re = 1.0$ . (A) pusher ( $\beta = -5$ ) for different  $Re$ . (B) puller ( $\beta = 5$ ) for different  $Re$ .

For the pusher as shown in (a), the positive and negative vorticity appear ahead and behind the pusher, and the opposite is true for the puller as shown in (b). There are small tip vortices at two poles of the squirmer with their direction being opposite to the adjacent main vorticity at  $Re = 0.01$ . For the pusher as shown in (a), the symmetry of the main vortex and tip vortex are broken more quickly with increasing  $Re$ . When upstream fluid flows through the pusher, the flow direction is consistent with that of fluid in the region with positive vorticity. Thus, upstream fluid is more likely to be attracted and accumulated in the region with positive vorticity, leading to a more engorged positive vorticity. Meanwhile, the fluid in the region with negative vorticity tends to escape from the control of viscous force and lacks the support of upstream fluid, resulting in a small and backward-extended negative vorticity at  $Re = 0.3$ . With the increase of  $Re$ , although the positive vorticity continues to grow, it also stretches back, causing more internal fluid to escape, with less exterior fluid entering this region. Thus, more upstream fluid enters the region with negative vorticity and the region grows at  $Re = 0.5$ . Finally, the regions with positive and negative vorticity are compressed and elongated at  $Re = 1.0$  and  $3.0$ . Similarly, the tip vortex with negative vorticity on the head of the pusher fades away due to the extrusion of upstream fluids, while the tip vortex with positive vorticity becomes larger due to the supplement of fluids which eliminates control of the main vortex with negative vorticity, and they extend as the main vortex does after saturating as shown in Figure 7a. Such a phenomenon can also be found for the puller as shown in Figure 7b, but there exist some differences: (1) Since the flow direction of the upstream fluids is opposite to that of fluids in the region with negative vorticity, the positive and negative vorticities are still approximately symmetric at  $Re = 0.01$ . With the increase of  $Re$ , the upstream fluids would rather stay in the region with positive vorticity than negative vorticity, which results in the positive vorticity being larger than the negative vorticity in the region behind the head of the puller at  $Re = 0.5$ . The region with negative vorticity is further squeezed to form a

pair of elongated vortexes on both sides of the puller at  $Re = 1.0$  and  $3.0$ . (2) The upstream fluids continuously flow into the tip vortex, leading to the collapse of the tip vortex with positive vorticity under overloads and breaking the swimming stability of the puller. The tip vortex with negative vorticity, however, is not affected because there is no direct impact from the upstream fluids shown in Figure 7b.

The relationship between velocity of the squirmer and  $Re$  for  $AR = 0.2$  is shown in Figure 8 where  $u^* = |u|/U$ ,  $Re$  corresponding to the data points is  $0.01, 0.05, 0.1, 0.3, 0.5, 0.7, 1.0$  and  $3.0$ , respectively. For the neutral squirmer ( $\beta = 0$ ),  $u^*$  does not vary with  $Re$ . The values of  $u^*$  of three kinds of squirmers are the same at  $Re = 0.01$ , i.e., there is no difference in  $u^*$  for different squirmers when the inertia is very small. With the increase of  $Re$ ,  $u^*$  increases monotonically and sharply when  $Re > 0.1$  for pusher, while  $u^*$  decreases from  $Re = 0.01$  to  $0.3$ , then increases from  $Re = 0.3$  to  $3$  for the puller. There exists a competition between viscous force and inertial force; upstream fluids flow downstream and accumulate at the head of the puller (in the region of the tip vortex in Figure 7 at  $Re = 0.01$ ), hindering the starting velocity of the puller.  $u^*$  of the puller increases when it begins to move, and the inertial force promotes  $u^*$  of the puller like that of the pusher. Moreover, the pulling mode of the puller will cause large resistance in swimming. Therefore, the stable velocity of the puller is always less than that of the pusher under the same inertial force.

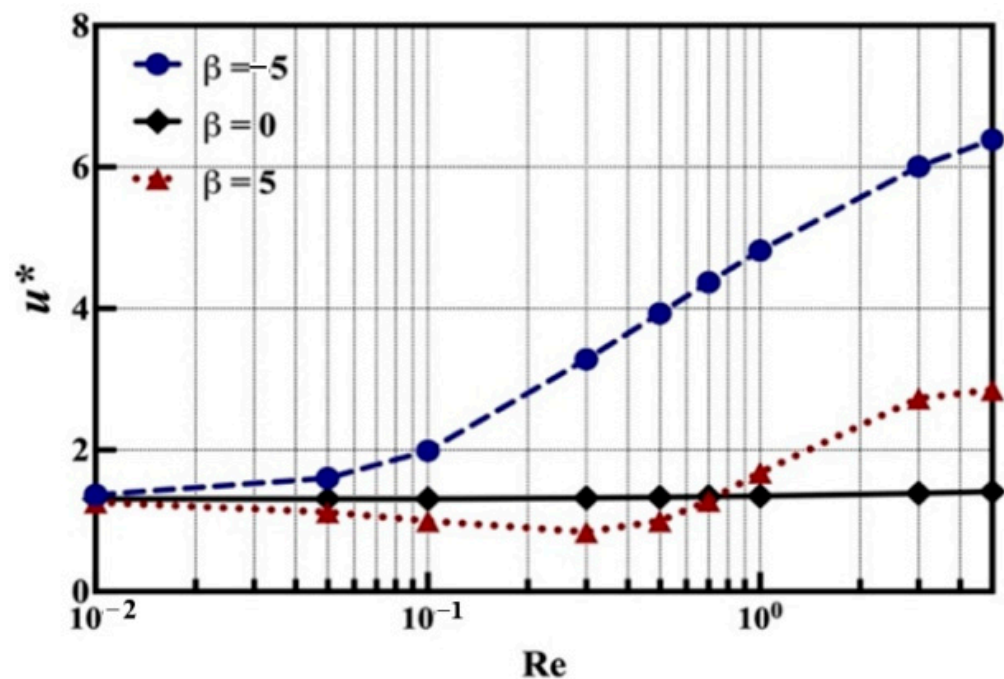


Figure 8. Relationship between  $u^*$  and  $Re$ .

The relationship between power expenditure  $P^*$  of the squirmer and  $Re$  for  $AR = 0.2$  is shown in Figure 9 where  $P^* = P/[(1 + \alpha)^2 B_1^2 \mu / 4]$  ( $P$  is power expenditure), and  $Re$  corresponding to the data points is  $0.01, 0.05, 0.1, 0.3, 0.5, 0.7, 1.0$  and  $3.0$ , respectively. The values of  $P^*$  of the pusher and puller are the same for  $0.01 \leq Re \leq 0.3$  because the squirmer mainly expends energy in overcoming viscous resistance in this range of  $Re$ .  $P^*$  increases with the increase of  $Re$  because the squirmer has to overcome more resistance caused by the inertia effect, and more power expenditure is needed. In addition, the values of  $P^*$  of the pusher are larger than those of the puller when  $Re > 0.3$ , which is in agreement with those for circular squirmers [9].

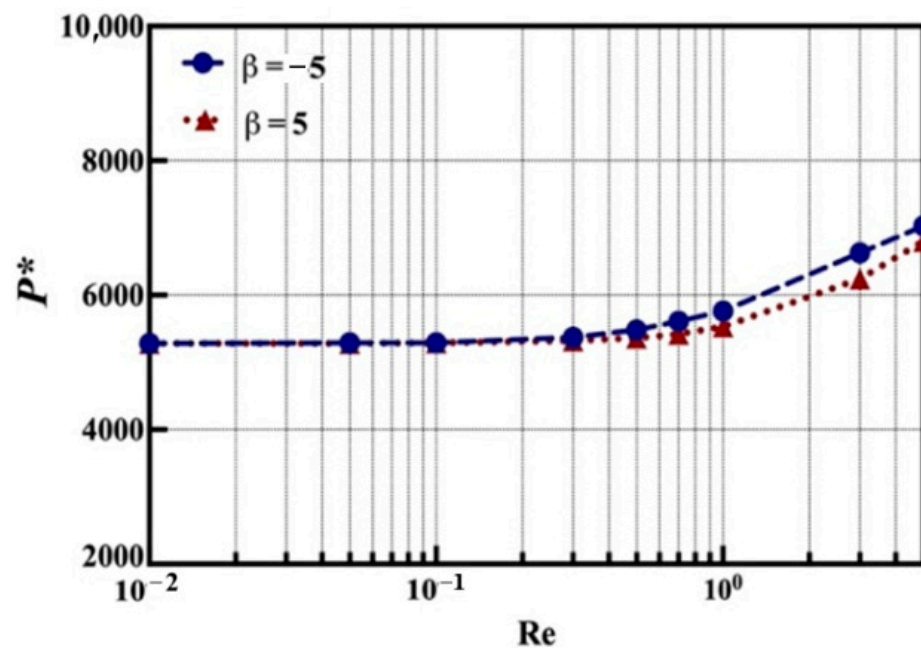


Figure 9. Relationship between  $P^*$  and  $Re$ .

The relationship between hydrodynamic efficiency  $\eta$  of the squirmer and  $Re$  for  $AR = 0.2$  is shown in Figure 10.  $\eta$  of the pusher and puller increases with increasing  $Re$ , but the pusher has a larger  $\eta$  than the puller under the same  $Re$ . Figure 11 shows the relationship between power-law exponent  $\gamma(u^* \sim (r^*)^{-\gamma})$  as shown in Figure 6 and  $Re$ . Combining Figures 10 and 11, we can see that fast velocity decay corresponds to large  $\eta$ , which is the same as the previous conclusion [13,33]. There exists a sudden reduction of  $\gamma$  for the puller at  $Re = 3.0$ ; this may be attributed to the breakage of the upstream tip vortex as shown in Figure 7.

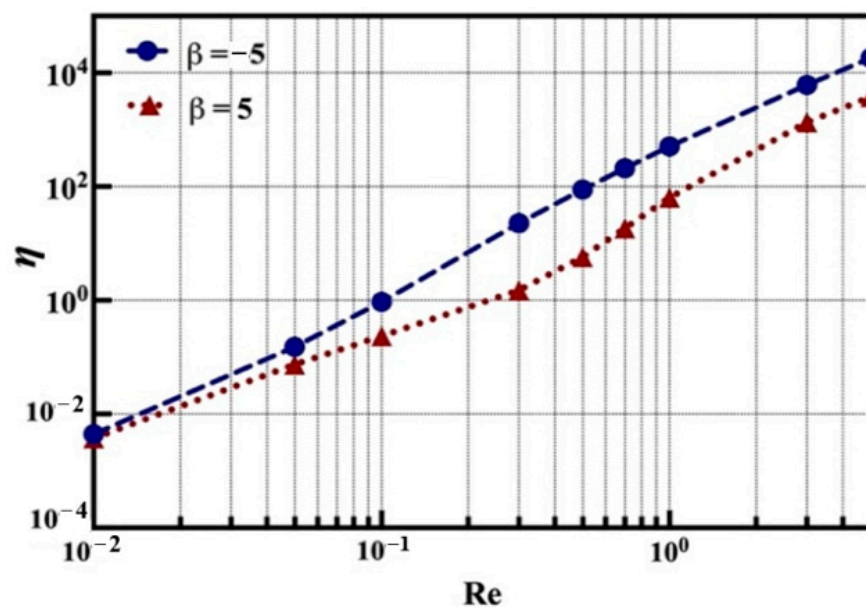


Figure 10. Relationship between  $\eta$  and  $Re$ .

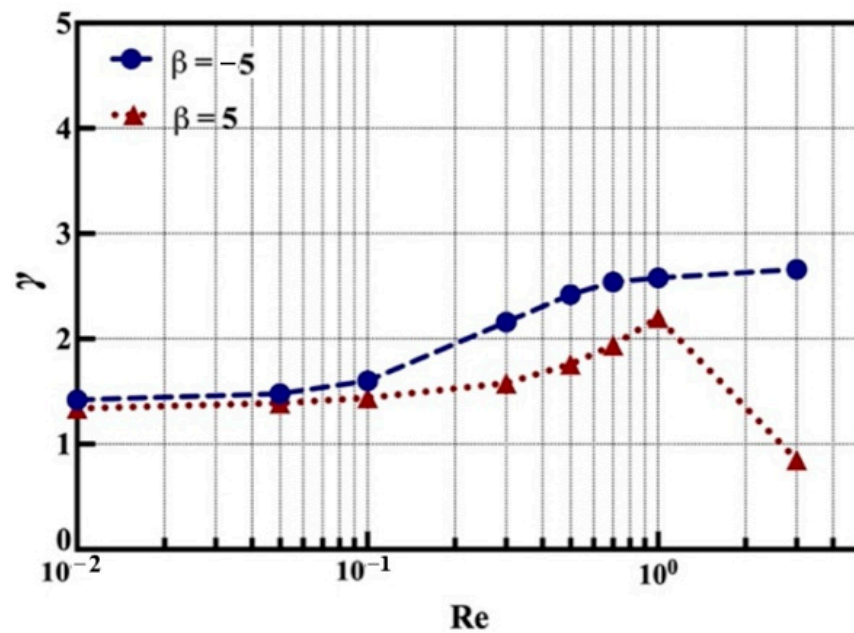


Figure 11. Relationship between  $\gamma$  and Re.

### 3.4. Effect of AR

As mentioned above, an elongated shape of the squirmer will lead to the generation of the tip vortex on both pole sides of the squirmer. The vortical contours induced by the squirmer with different AR are shown in Figure 12 where the definition of positive and negative vorticity is the same as Figure 7, and the contour range is  $-10^{-3} \sim 10^{-3}$ .

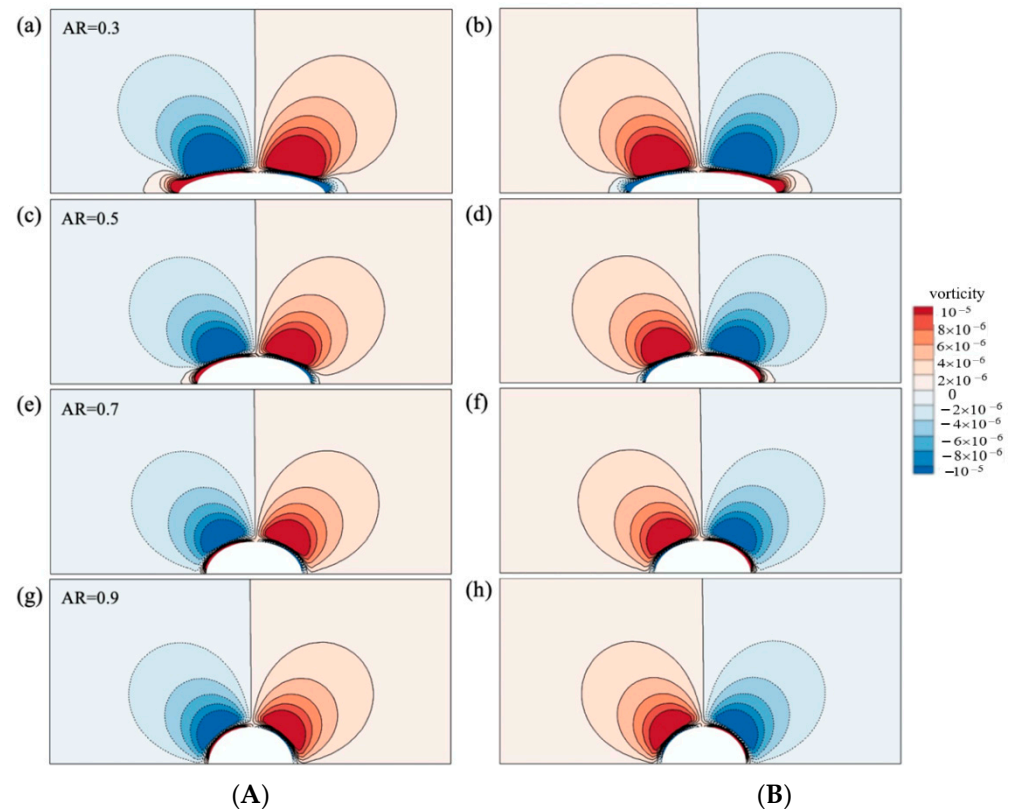


Figure 12. Vortical contours induced by elliptical squirmer with different AR at  $Re = 0.01$ . (a,b)  $Re = 0.3$ , (c,d)  $Re = 0.5$ , (e,f)  $Re = 0.7$ , (g,h)  $Re = 0.9$ . (A) pusher ( $\beta = -5$ ) for different AR. (B) puller ( $\beta = 5$ ) for different AR.

The tip vortex appears at both tips of the squirmer (like wing tip vortex) for  $AR = 0.3$ . This can be attributed to the separation of flow in the tip of the squirmer because the fluid more easily eliminates the attraction of the squirmer's surface and changes its flow direction in the tip. The tip vortex disappears gradually with increasing  $AR$  because the fluid is more likely to move along the surface of the squirmer through the control of viscous force, and it is difficult for the tip vortex to form. Moreover, the distributions of positive and negative vorticity are fore-aft symmetric at low  $Re$ .

Relationships between  $u^*$ ,  $P^*$ ,  $\eta$  of squirmer and  $AR$  at  $Re = 0.01$  are shown in Figures 13–15, respectively.  $u^*$  and  $P^*$  decrease with increasing  $AR$  (i.e., tending to be round). The pusher and puller have the largest and least  $u^*$ , respectively, as shown in Figure 13. The values of  $P^*$  of the pusher and puller are almost the same and are much larger than those of the neutral squirmer as shown in Figure 14. As shown in Figure 15,  $\eta$  increases for the neutral squirmer, but changes non-monotonically for the pusher and puller with the increase of  $AR$ . A specific analysis of this phenomenon should be made. Smaller  $AR$  corresponds to a larger contact area between the squirmer and fluid, so that there is larger friction resistance. The friction resistance is the main source of drag force at low  $Re$  [34], so the squirmer with small  $AR$  ( $AR = 0.3$ ) has to spend more energy to swim, resulting in the reduction of  $\eta$ . For the squirmer with larger  $AR$ , the resistance induced by pressure difference is relatively large and should be considered. Therefore,  $\eta$  is dependent on the relative contribution of friction resistance and resistance induced by pressure difference.

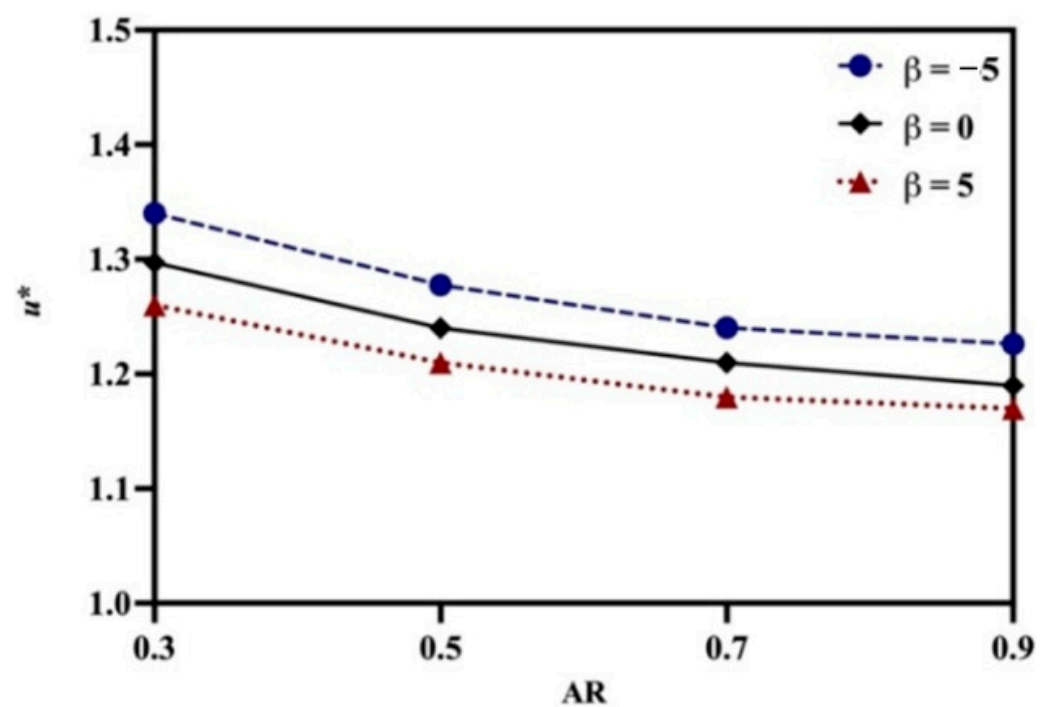


Figure 13. Relationship between  $u^*$  and  $AR$ .

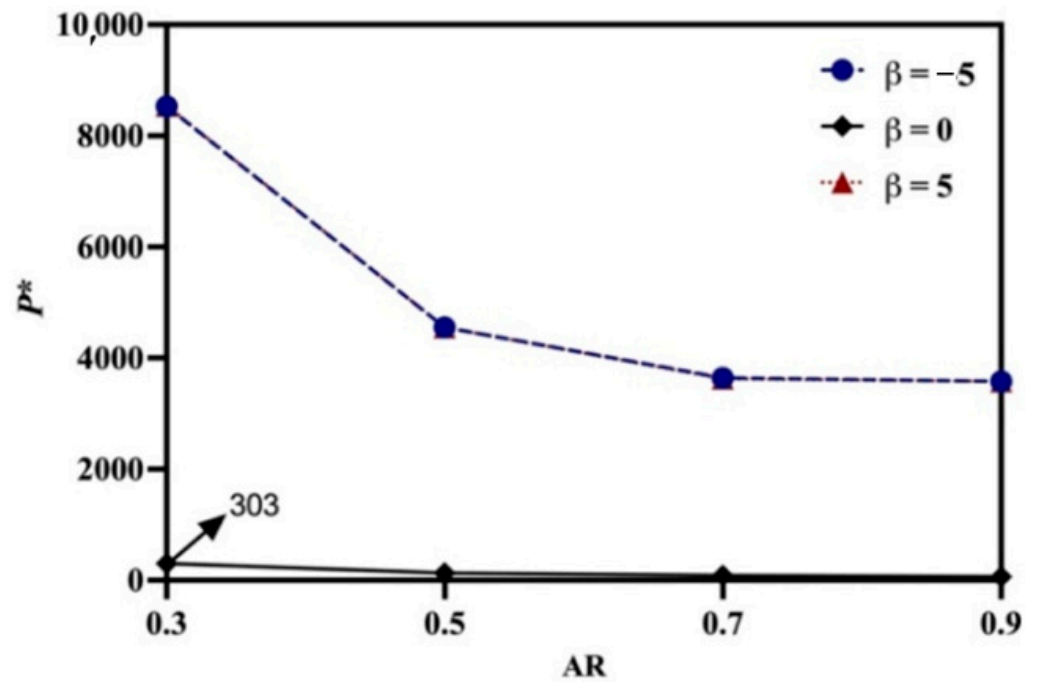


Figure 14. Relationship between  $P^*$  and AR.

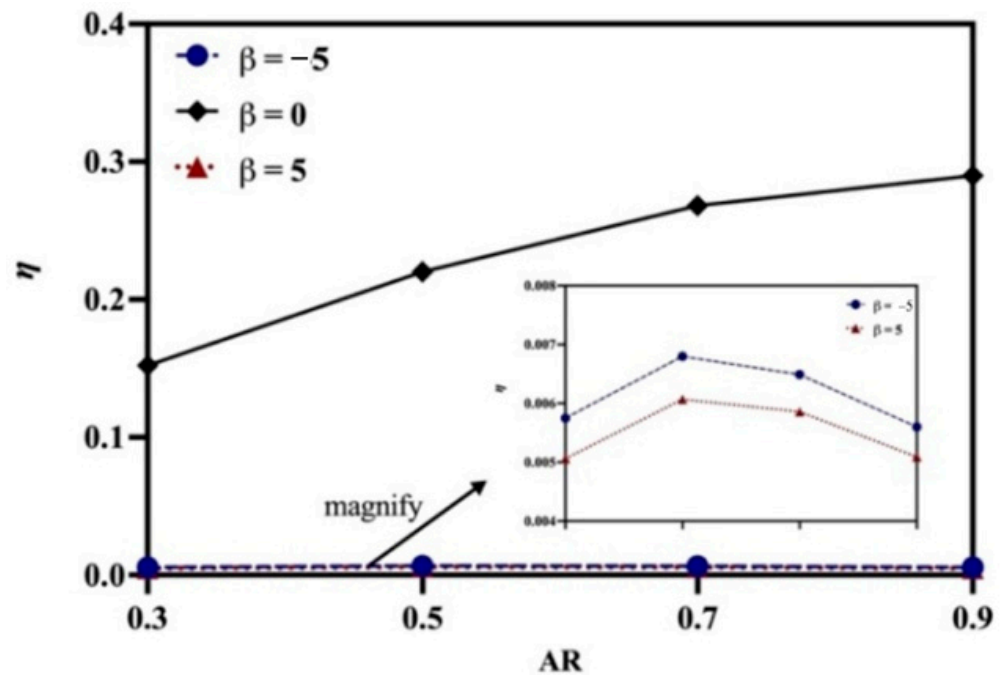


Figure 15. Relationship between  $\eta$  and AR.

#### 4. Conclusions

In this paper, a tangential velocity model for the elliptical squirmer is proposed based on the circular squirmer model and the conformal-mapping technique, and the hydrodynamic characteristics of the squirmer are simulated numerically using the IB-LBM. The feasibility of the numerical scheme and code is validated by comparing the present results with previous ones. The streamline, velocity and vorticity induced by the squirmer with different Re and AR are analyzed. The effects of Re and AR on  $u^*$ ,  $P^*$  and  $\eta$  are explored. The main conclusions are summarized as follows:

(1) The streamline and velocity are fore-aft symmetric for the neutral squirmer, but not for the pusher and puller. The change of  $u^*$  along the radial direction shows the relation of  $u^* \sim r^{*-2}$  for the neutral squirmer, and  $u^* \sim r^{*-1}$  for the pusher and puller. For the pusher, there are small tip vortexes at two poles at  $Re = 0.01$ . The symmetry of the main and tip vortexes is broken more quickly with increasing  $Re$ . There exists a small and backward-extended region with negative vorticity at  $Re = 0.3$ ; the region expands at  $Re = 0.5$ , and the regions with positive and negative vorticity are compressed and elongated at  $Re = 1.0$  and  $3.0$ . The tip vortex with negative vorticity on the head fades away, while the tip vortex with positive vorticity becomes larger. The above phenomenon for the pusher also occurs for the puller, but there are some differences. For the puller, the distributions of positive and negative vorticity are still approximately symmetric at  $Re = 0.01$ , the positive vorticity is larger than the negative vorticity in the region behind the head at  $Re = 0.5$ , and the region with negative vorticity is further squeezed to form a pair of elongated vortexes on both sides at  $Re = 1.0$  and  $3.0$ . The tip vortex with positive vorticity collapses, but the tip vortex with negative vorticity is not affected.

(2) For the neutral squirmer,  $u^*$  does not vary with  $Re$ , and there is no difference in  $u^*$  for different squirmers at small  $Re$ . With the increase of  $Re$ ,  $u^*$  of the pusher increases monotonically, but  $u^*$  of the puller decreases from  $Re = 0.01$  to  $0.3$ , and then increases from  $Re = 0.3$  to  $3$ .  $u^*$  of the puller is always less than that of the pusher at the same  $Re$ . The values of  $P^*$  of the pusher and puller are the same for  $0.01 \leq Re \leq 0.3$ ,  $P^*$  of the pusher is larger than that of the puller when  $Re > 0.3$ , and  $P^*$  increases with increasing  $Re$ .  $\eta$  of the pusher and puller increases with increasing  $Re$ , but the pusher has a larger  $\eta$  than the puller at the same  $Re$ .

(3) The tip vortexes appear at both tips of the squirmer for  $AR = 0.3$ , and disappear gradually with increasing  $AR$ . The distributions of positive and negative vorticity are fore-aft symmetric at low  $Re$ .  $u^*$  and  $P^*$  decrease with increasing  $AR$ . The pusher and puller have the largest and least  $u^*$ , respectively. The values of  $P^*$  of the pusher and puller are almost the same and are much larger than those of the neutral squirmer. With the increase of  $AR$ ,  $\eta$  increases for the neutral squirmer, but changes non-monotonically for the pusher and puller.  $\eta$  is dependent on the relative contribution of friction resistance and resistance induced by pressure difference.

**Author Contributions:** Conceptualization, C.L. and J.L.; methodology, C.L., P.Z. and Z.O.; software, C.L., P.Z. and Z.O.; validation, C.L. and P.Z.; formal analysis, C.L., J.L. and Z.O.; investigation, C.L., P.Z. and J.L.; resources, C.L. and Z.O.; data curation, C.L.; writing—original draft preparation, C.L. and P.Z.; writing—review and editing, J.L.; visualization, Z.O.; supervision, J.L.; project administration, J.L.; funding acquisition, J.L. All authors have read and agreed to the published version of the manuscript.

**Funding:** National Natural Science Foundation of China (Grant: 12132015).

**Institutional Review Board Statement:** Not applicable.

**Informed Consent Statement:** Not applicable.

**Data Availability Statement:** Not applicable.

**Conflicts of Interest:** The authors declare no conflict of interest.

## Nomenclature

$c_s$	sound speed	$D$	discrete delta function
$\mathbf{e}_\alpha$	unit direction vector	$\mathbf{f}$	external force density
$f_\alpha$	particle distribution function	$f_\alpha^{eq}$	equilibrium distribution function
$\mathbf{F}_b$	force density	$h$	mesh spacing
$F_\alpha$	discrete force distribution function	$\mathbf{n}$	normal vector to squirmer surface
$\mathbf{U}$	fluid velocity	$\mathbf{u}_b^{noF}$	unforced velocity
$U$	stable squirmer velocity	$\mathbf{v}_\theta$	tangential velocity at boundary
$w_\alpha$	weight associated with $\mathbf{e}_\alpha$	$\Delta s_b$	arc length of boundary segment
$\Delta t$	unit lattice time	$\eta$	hydrodynamic efficiency
$M$	fluid viscosity	$\rho$	fluid density
$\rho_b^{noF}$	unforced density	$\sigma$	stress tensor
$\tau$	dimensionless relaxation time	$\varphi$	rotation angle of squirmer

## References

- Liu, C.; Lin, J.Z. A review on the some issues of multiphase flow with self-driven particles. *Appl. Sci.* **2021**, *11*, 7361. [\[CrossRef\]](#)
- Lighthill, M.J. On the squirming motion of nearly spherical deformable bodies through liquids at very small reynolds numbers. *Commun. Pure Appl. Math.* **1952**, *5*, 109–118. [\[CrossRef\]](#)
- Blake, J.R. A spherical envelope approach to ciliary propulsion. *J. Fluid Mech.* **1971**, *46*, 199–208. [\[CrossRef\]](#)
- Blake, J.R. Self propulsion due to oscillations on the surface of a cylinder at low reynolds number. *Bull. Aust. Math. Soc.* **1971**, *5*, 255–264. [\[CrossRef\]](#)
- Ishikawa, T.; Pedley, T.J. Coherent structures in monolayers of swimming particles. *Phys. Rev. Lett.* **2008**, *100*, 088103. [\[CrossRef\]](#) [\[PubMed\]](#)
- Magar, V.; Pedley, T.J. Average nutrient uptake by a self-propelled unsteady squirmer. *J. Fluid Mech.* **2005**, *539*, 93. [\[CrossRef\]](#)
- Ishikawa, T.; Simmonds, M.; Pedley, T.J. Hydrodynamic interaction of two swimming model micro-organisms. *J. Fluid Mech.* **2006**, *568*, 119–160. [\[CrossRef\]](#)
- Ishikawa, T.; Pedley, T.J. The rheology of a semi-dilute suspension of swimming model micro-organisms. *J. Fluid Mech.* **2007**, *588*, 399–435. [\[CrossRef\]](#)
- Ouyang, Z.; Lin, J.Z.; Ku, X. The hydrodynamic behavior of a squirmer swimming in power-law fluid. *Phys. Fluids* **2018**, *30*, 083301. [\[CrossRef\]](#)
- Ouyang, Z.; Lin, J.Z.; Ku, X. Hydrodynamic properties of squirmer swimming in power-law fluid near a wall. *Rheol. Acta* **2018**, *57*, 655–671. [\[CrossRef\]](#)
- Ouyang, Z.; Lin, J.Z.; Ku, X. Hydrodynamic interaction between a pair of swimmers in power-law fluid. *Int. J. Non-Linear Mech.* **2019**, *108*, 72–80. [\[CrossRef\]](#)
- Ouyang, Z.; Lin, J.Z. Migration of a micro-swimmer in a channel flow. *Powder Technol.* **2021**, *392*, 587–600. [\[CrossRef\]](#)
- Zantop, A.W.; Stark, H. Squirmer rods as elongated microswimmers: Flow fields and confinement. *Soft Matter* **2020**, *16*, 6400–6412. [\[CrossRef\]](#) [\[PubMed\]](#)
- Ouyang, Z.; Phan-Thien, N. Inertial swimming in a channel filled with a power-law fluid. *Phys. Fluids* **2021**, *33*, 113312. [\[CrossRef\]](#)
- Ouyang, Z.; Lin, J.Z. The Hydrodynamics of an inertial squirmer rod. *Phys. Fluids* **2021**, *33*, 073302. [\[CrossRef\]](#)
- Blake, J. A Model for the micro-structure in ciliated organisms. *J. Fluid Mech.* **1972**, *55*, 1–23. [\[CrossRef\]](#)
- Blake, J. A Finite model for ciliated micro-organisms. *J. Biomech.* **1973**, *6*, 133–140. [\[CrossRef\]](#)
- Keller, S.R.; Wu, T.Y. A porous prolate-spheroidal model for ciliated micro-organisms. *J. Fluid Mech.* **1977**, *80*, 259–278. [\[CrossRef\]](#)
- Theers, M.; Westphal, E.; Gompper, G.; Winkler, R.G. Modeling a spheroidal microswimmer and cooperative swimming in thin films. *Soft Matter* **2016**, *12*, 7372–7385. [\[CrossRef\]](#)
- Theers, M.; Westphal, E.; Qi, K.; Winkler, R.G.; Gompper, G. Clustering of microswimmers: Interplay of shape and hydrodynamics. *Soft Matter* **2018**, *14*, 8590–8603. [\[CrossRef\]](#)
- Shapere, A.; Wilczek, F. Geometry of self-propulsion at low reynolds number. *J. Fluid Mech.* **1989**, *198*, 557–585. [\[CrossRef\]](#)
- Leshansky, A.M.; Kenneth, O.; Gat, O.; Avron, J.E. A frictionless microswimmer. *New J. Phys.* **2007**, *9*, 145. [\[CrossRef\]](#)
- Kang, S.K.; Hassan, Y.A. A comparative study of direct-forcing immersed boundary-lattice Boltzmann methods for stationary complex boundaries. *Int. J. Numer. Methods Fluids* **2011**, *66*, 1132–1158. [\[CrossRef\]](#)
- Yang, X.; Zhang, X.; Li, Z.; He, G.W. A Smoothing technique for discrete delta functions with application to immersed boundary method in moving boundary simulations. *J. Comput. Phys.* **2009**, *228*, 7821–7836. [\[CrossRef\]](#)
- Choudhary, A.; Paul, S.; Ruhle, F.; Stark, H. How inertial lift affects the dynamics of a microswimmer in Poiseuille flow. *Commun. Phys.* **2022**, *5*, 14. [\[CrossRef\]](#)
- Avron, J.E.; Gat, O.; Kenneth, O. Optimal swimming at low reynolds numbers. *Phys. Rev. Lett.* **2004**, *93*, 186001. [\[CrossRef\]](#)
- Feng, J.; Hu, H.H.; Joseph, D.D. Direct simulation of initial value problems for the motion of solid bodies in a newtonian fluid part 1. sedimentation. *J. Fluid Mech.* **1994**, *261*, 95–134. [\[CrossRef\]](#)

28. Feng, Z.G.; Michaelides, E.E. Interparticle forces and lift on a particle attached to a solid boundary in suspension flow. *Phys. Fluids* **2002**, *14*, 49–60. [[CrossRef](#)]
29. Feng, Z.G.; Michaelides, E.E. The immersed boundary-lattice boltzmann method for solving fluid–particles interaction problems. *J. Comput. Phys.* **2004**, *195*, 602–628. [[CrossRef](#)]
30. Pöhl, R.; Popescu, M.N.; Uspal, W.E. Axisymmetric spheroidal squirmers and self-diffusiophoretic particles. *J. Phys. Condens. Matter* **2020**, *32*, 164001. [[CrossRef](#)]
31. Andreoni, W.; Yip, S. *Handbook of Materials Modeling: Methods: Theory and Modeling*; Springer: Berlin/Heidelberg, Germany, 2020.
32. Chisholm, N.G.; Legendre, D.; Lauga, E.; Khair, A.S. A squirmer across reynolds numbers. *J. Fluid Mech.* **2016**, *796*, 233–256. [[CrossRef](#)]
33. Zhu, L.; Do-Quang, M.; Lauga, E.; Brandt, L. Locomotion by tangential deformation in a polymeric fluid. *Phys. Rev. E* **2011**, *83*, 011901. [[CrossRef](#)] [[PubMed](#)]
34. Nejat, A.; Mirzakhali, E.; Aliakbari, A.; Niasar, M.S.F.; Vahidkhah, K. Non-newtonian power-law fluid flow and heat transfer computation across a pair of confined elliptical cylinders in the line array. *J. Non-Newton. Fluid Mech.* **2012**, *171–172*, 67–82. [[CrossRef](#)]